ACS OMEGA

http://pubs.acs.org/journal/acsodf

Article

Square-Facet Nanobar MOF-Derived Co_3O_4@Co/N-doped CNT Core–Shell-based Nanocomposites as Cathode Materials for High-Performance Supercapacitor Studies

Swapnajit V. Mulik, Suprimkumar D. Dhas, Annasaheb V. Moholkar, Vinayak G. Parale, Hyung-Ho Park, Pramod A. Koyale, Vijay S. Ghodake, Dillip K. Panda, and Sagar D. Delekar*

Cite This: *ACS Omega* 2023, 8, 2183–2196

Read Online

ACCESS | Metrics & More | Article Recommendations | Supporting Information

ABSTRACT: The binary as well as ternary nanocomposites of the square-facet nanobar Co-MOF-derived Co_3O_4@Co/N-CNTs (N-CNTs: nitrogen-doped carbon nanotubes) with Ag NPs and rGO have been synthesized via an easy wet chemical route, and their supercapacitor behavior was then studied. At a controlled pH of the precursor solution, square-facet nanobars of Co-MOF were first synthesized by the solvothermal method and then pyrolyzed under a controlled nitrogen atmosphere to get a core–shell system of Co_3O_4@Co/N-CNTs. In the second step, different compositions of Co_3O_4@Co/N-CNT core–shell structures were formed by an *ex-situ* method with Ag NPs and rGO moieties. Among several bare, binary, and ternary compositions tested in 6 M aqueous KOH electrolyte, a ternary nanocomposite having a 7.0:1.5:1.5 stoichiometric ratio of Co_3O_4@Co/N-CNT, Ag NPs, and rGO, respectively, reported the highest specific capacitance (3393.8 F g^{-1} at 5 mV s^{-1}). The optimized nanocomposite showed the energy density, power density, and Coulombic efficiency of 74.1 W h.kg^{-1}, 443.7 W.kg^{-1}, and 101.3%, respectively, with excellent electrochemical stability. After testing an asymmetrical supercapacitor with a Co_3O_4@Co/N-CNT/Ag NPs/rGO/nickel foam cathode and an activated carbon/nickel foam anode, it showed 4.9 W h.kg^{-1} of energy density and 5000.0 W.kg^{-1} of power density.

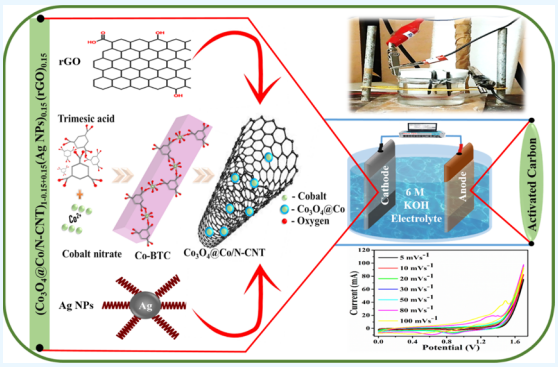

INTRODUCTION

Batteries and capacitors exhibit high energy density and high power density, respectively, but a supercapacitor's performance is in between them.[1] Recently, researchers have focused on creating high energy density materials for electrodes, with the aim of elevating supercapacitors to battery-level energy density.[2,3] In connection with this, development of better electrode materials for supercapacitors, including transition-metal oxides (TMOs) and their composites, has attracted significant scientific attention.[4,5] TMOs are considered promising electrode materials for supercapacitors due to their remarkable properties such as high energy density (10 to 100 times that of electrolytic capacitors), excellent reversibility (surface properties), abundant redox-active reserves, and high theoretical capacitance.[1,4−8]

For energy storage devices to be optimized for good electrochemical performance, an electrode material with a well-defined structure with controllable morphology as well as porous nature is supposed to be an important candidate.[9,10] Metal oxides having a porous nature can provide more redox-active sites, enhancing the electrochemical supercapacitor performance.[11,12] Hence, metal–organic framework (MOF)-derived TMOs in nanoscale dimensions are becoming progressively important in the field of supercapacitors. MOFs are materials having a wide variety of structures, tunable shapes, porosity, and so forth.[13,14] As a result, MOFs can be used as precursors for TMO synthesis.[15] MOF-derived TMOs have a highly porous nature, which improves the structural stability and surface area, shortens the diffusion path of electrolyte ions, and reduces resistance to ion diffusion.[16] From MOF precursors, various highly porous TMO nanomaterials have been derived for supercapacitor applications, including cuprous oxide (Cu_2O; C_s: 365.0 F g^{-1}) [C_s = specific capacitance],[17] cobalt oxide (Co_3O_4; C_s: 508.0 F g^{-1}),[18] manganese oxide (Mn_3O_4@C; C_s: 162.6 F g^{-1}),[11] nickel oxide (NiO; C_s: 324.0 F g^{-1}),[19] and so forth. Among these TMOs, Co_3O_4 has been exploited very well due to its good electrochemical stability, high theoretical capacitance (~3600 F g^{-1}), low cost, and high abundance.[20] All these achievements notwithstanding, MOF-derived Co_3O_4 exhibits numerous

Received: October 3, 2022
Accepted: November 29, 2022
Published: January 4, 2023

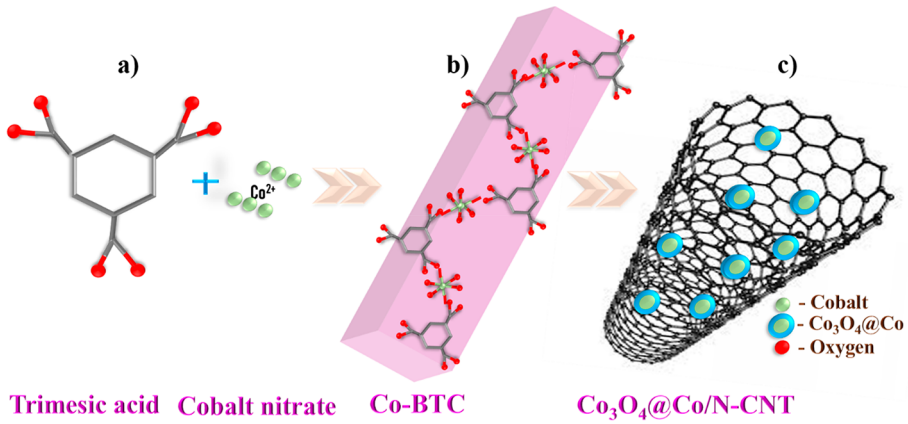

Figure 1. Schematic illustration of (a) precursors for the synthesis of Co-BTC, (b) square-facet Co-BTC nanobars, and (c) calcination of Co-BTC leading to the formation of Co_3O_4@Co/N-CNT.

shortcomings in terms of electronic conductivity, cycle life, rate capability, and electron kinetics.[21] As a result of the reported research endeavors, it was seen that the observed electrochemical properties of MOF-derived Co_3O_4 are still obscure, so investigators have adopted various strategies, such as compositing TMOs for enhancing the electrochemical performance, doping for enhancing capacitance values, tuning the morphology for better exploration of redox-active sites, and so forth.[20−23] Therefore, among different strategies, forming composites between MOF-derived Co_3O_4 and carbonaceous materials is to be developed,[23] where the carbonaceous materials act as supporting material for achieving better stability as well as electrochemical properties than bare TMOs in supercapacitors.[11,22,23] Additionally, volume changes of bare or composite electrode materials are also reduced by the carbon matrix by its synergistic effect with the pseudocapacitive and electric double-layer mechanism.[24]

With these motivations in mind, researchers are compositing TMOs with carbonaceous matrixes to develop high-performance electrochemical supercapacitors.[25] These hybrid materials possess outstanding chemical and physical properties.[26] Reduced graphene oxide (rGO) has a high surface area (2630 $m^2\ g^{-1}$), high stability, abundant reactive sites, and other properties that make it a promising active supportive material for the development of supercapacitors.[27] Additional benefits of rGO include its higher ballistic conductivity (103.3 S cm^{-1}) and better charge-transfer properties.[28,29] Literature studies have also illustrated how TMO−rGO composites such as Co_3O_4/N-rGO and 3D rGO-Co_3O_4 enhance the conductivity and charge−discharge cycle stability.[30,31] Furthermore, the high surface area of rGO materials allows higher contact between electrolyte ions and electrodes for better electrode chemistry.[26−31]

Despite the improved properties of the composites between MOF-derived Co_3O_4 and rGO, the resulting binary composites suffer from internal resistance during electrochemical performance tests.[32] This causes capacitance values to lag behind theoretical values. A favorable strategy to overcome this challenge would therefore be to load silver nanoparticles (Ag NPs) on the surface of binary Co_3O_4−rGO composites.[33−35] By loading Ag NPs onto other composites, additional redox reactions occur due to multiple oxidation states of Ag NPs with enhancement in chemical as well as thermal stability, which synergize to improve the electrochemical performance of the host composites.[36] Due to this, the ternary composites between Co_3O_4 with rGO and Ag NPs would have excellent supercapacitive performance.[37−39] Also, it is particularly important to create core−shell materials with as many reserved electrons as possible in the core of Co_3O_4 for boosting the conductivity.[40]

Hence, we report a strategy to synthesize square-facet Co-MOF nanobar templates by using a solvothermal method at a controlled pH. Finally, we use the Co-MOF templates to synthesize porous Co_3O_4@Co/N-CNT core−shell materials, which are further utilized for preparing binary as well as ternary nanocomposites (NCs) with Ag NPs and rGO. After physicochemical property testing of the prepared NCs, the electrochemical performance is measured using an aqueous asymmetric supercapacitor device.

EXPERIMENTAL SECTION

Materials. All chemicals were of analytical grade and used as received without further purification. Cobalt nitrate ($Co(NO_3)_2{\cdot}6H_2O$, 99%), trimesic acid [benzene tricarboxylate (BTC), 95%], ethanol (C_2H_6O, ∼99.8%), *N*,*N*-dimethylformamide (DMF, 99%), ammonia (NH_3, 25%), *N*-methyl-2-pyrrolidinone (C_5H_9NO, 99.5%), polyvinylidene difluoride (PVDF), potassium hydroxide (KOH, ≥85%), and so forth were purchased from Sigma-Aldrich and Merck Company.

A suspension of Ag NPs was made by using a reported method (ref[41]), while functionalization of rGO was carried out as per the standard reported method;[42] both the experimental protocols are reported in Supporting Information.

Synthesis of Square-Facet Co-MOF Nanobars. In a typical synthesis, the $Co(NO_3)_2{\cdot}6H_2O$ (0.01 M) aqueous solution was mixed with BTC (0.005 M in DMF), and the suspension was ultrasonically dispersed for 30 min. Under constant stirring for 3 h., ammonia was added to the precursor solution to adjust the pH (pH = 6 ± 0.10) of the resulting solution. Then, the resultant solution was calcined in a stainless autoclave lined with Teflon at 120 °C for 10 h. The obtained precipitate was centrifuged, washed with distilled water followed by ethanol, and dried at 60 °C for 8 h. Different characterization tools were used to characterize the precipitate of the square-facet Co-BTC nanobars complex.

Synthesis of MOF-Derived Core−Shell Co_3O_4@Co/N-CNT (CNC). Square-facet Co-BTC nanobars were pyrolyzed at 600 °C (10 °C min^{-1}) for 2 h under a N_2 atmosphere. Then, the desired materials were cooled to 200 °C, and then the two ends of the furnace were opened for mild calcination for 3 h to

https://doi.org/10.1021/acsomega.2c06369
ACS Omega 2023, 8, 2183−2196

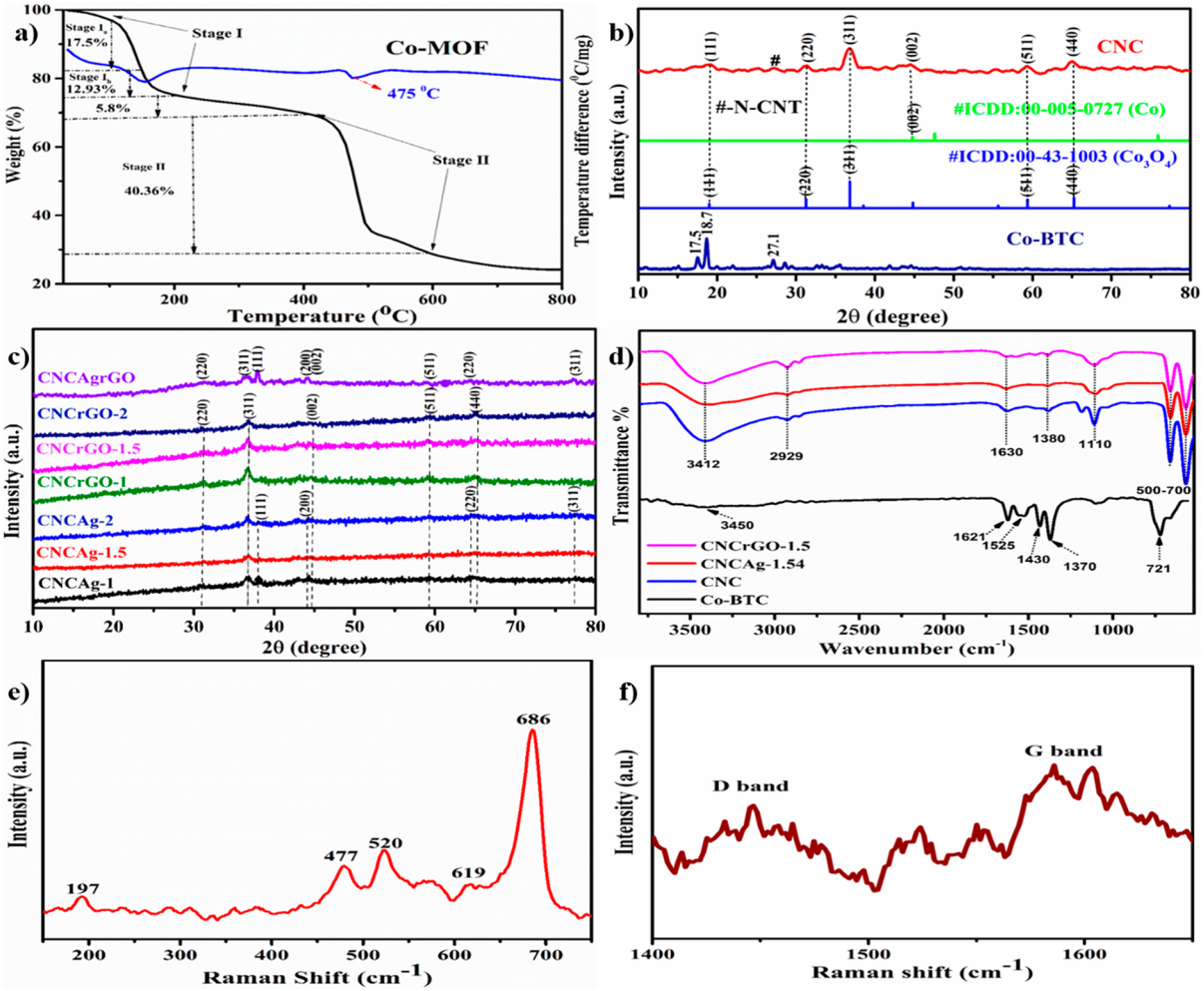

Figure 2. (a) TG analysis of Co-BTC MOF; (b) XRD patterns of Co-BTC, CNC with simulated patterns of Co_3O_4 (#ICDD: 00-43-1003), and Co (#ICDD:00-005-0727); (c) XRD patterns of binary CNCAg-1, CNCAg-1.5, CNCAg-2, CNCrGO-1, CNCrGO-1.5, CNCrGO-2, and ternary CNCAgrGO NCs; (d) FT-IR spectra of Co-BTC, CNC, CNCAg-1.5, and CNCrGO-1.5; and (e,f) Raman spectra of CNC.

get the core−shell form of the resulting CNC. Figure 1 shows the schematic for the synthesis of Co-MOF-derived CNC.

Synthesis of Binary NCs between Co_3O_4@Co/N-CNT and Other Supportive Materials (Ag NPs and rGO). In *ex-situ* protocol, binary $(CNC)_{1-x}(Ag)_x$ NCs were prepared with varying contents of the as-synthesized Ag NPs (x = 10, 15, and 20 wt %). After dispersing CNC in ethanol using ultrasonication for 40 min, the dispersion of Ag NPs was added to the previously dispersed CNC.[43] The resulting mixture was further dispersed using ultrasonication for 40 min. Afterward, the composite was dried at 80 °C for 2 h. Based on the content of Ag NPs, the prepared NCs are labeled as CNCAg-1, CNCAg-1.5, and CNCAg-2 with respect to 10, 15, and 20 wt % of Ag content in the NCs.

A similar protocol was adopted for preparing binary NCs using varying contents of rGO (10, 15, and 20 wt %), and the respective NCs were labeled as CNCrGO-1, CNCrGO-1.5, and CNCrGO-2.

Synthesis of Ternary $(Co_3O_4$@Co/N-CNT$)_{1-(x+y)}$ (Ag NPs$)_x$(rGO$)_y$ NCs. Ternary NCs were prepared by mixing the respective dispersed amounts of CNC with Ag NPs and rGO in ethanol using an ultrasonicator for 40 min. The ethanol was subsequently evaporated using a hot plate, and then the NCs were dried at 80 °C for 2 h. Fine powder of the ternary NCs was obtained through grinding using a mortar and pestle, thus preparing ternary $(CNC)_{1-0.15+0.15}(Ag\ NPs)_{0.15}(rGO)_{0.15}$ NCs labeled as CNCAgrGO.

Fabrication of the Working Electrode. Initially, nickel foam (NF) substrates (1 × 3 cm) were first etched in HCl solution (3 M) and then washed with acetone to remove impurities present on their surface. A homogeneous slurry was prepared by mixing CNC or its NCs with super-P (conducting carbon) and PVDF (binder) in a ratio of 8:1:1 wt %. In the first step, PVDF was dissolved in the NMP solvent; then, appropriate amounts of materials (CNC or its NCs and super-P) were added slowly under constant stirring so as to form a slurry of the NCs. The prepared slurry was applied to the NF (thickness = 1 mm, and area = 1 cm^2) substrate using the drop-casting method. Then, the deposited NF electrode was dried at 90 °C for 10 h.

Materials Characterization. Thermogravimetric (TG) analysis of the Co-BTC template was performed using a TA thermal analyzer instrument under a controlled N_2 atmosphere at a heating rate of 10 °C min^{-1}. Powder X-ray diffraction (XRD) patterns of the samples were obtained using a Bruker AXS diffractometer D2 model. Microscopic analyses of the samples were carried out with field-emission scanning electron microscopy (FESEM-JEOL JSM 7001F, Japan and MIRA3

https://doi.org/10.1021/acsomega.2c06369
ACS Omega 2023, 8, 2183−2196

TESCAN) as well as high-resolution transmission electron microscopy (TEM JEM-2100F JEOL, Japan) operating at 125 kV. FT-IR spectra were obtained on an infrared spectrometer (Bruker Alpha FT9). Crystallinity and molecular interactions study was carried out using Raman spectroscopy (Bruker MultiRAM, Germany). X-ray photoelectron spectra of the samples were recorded using an XPS spectrometer with a K-alpha, Thermo VG, UK) spectrometer and an Al X-ray source (Kα line: 1486.6 eV, 3 mA, and 12 kV). The surface area was investigated using the Brunauer–Emmett–Teller (BET) method on a NOVA 1000e Quantachrome, and the Barrette–Joyner–Halenda (BJH) algorithm was applied to understand the pore size distribution branch of the isotherm.

Electrochemical Measurements. The different electrochemical measurements, including cyclic voltammetry (CV) studies, galvanostatic charge/discharge (GCD) studies, and electrochemical impedance study (EIS) of the bare as well as NCs were carried out using a potentiostat VMP3 (BioLogic, France) electrochemical analyzer. All these measurements were carried out using a three-electrode system, consisting of a saturated calomel electrode as reference electrode, platinum as counter electrode (CE), and a working electrode (WE) consisting of bare or NCs deposited on NF with 6 M KOH electrolyte solutions.

Specific capacitance of the materials was calculated using eqs 1 and 2 based on CV and GCD data, respectively.

$$\text{Specific capacitance } (C_s) = \frac{A}{2mk\Delta V} \quad (1)$$

$$\text{Specific capacitance } (C_s) = \frac{I \times \Delta t}{\Delta V \times m} \quad (2)$$

where A is the area under the CV curve, m is the mass of the active electrode material, k is the scan rate, ΔV is the potential window, I is the current applied, and $T_d/\Delta t$ is discharge time. Additionally, the energy density (E_d) (W h kg^{-1}) and power density (P_d) (W kg^{-1}) as well as the Coulombic efficiency (η) of the materials were calculated from eqs 3–5, respectively.

$$E_d = \frac{1}{2 \times 3.6} C_s (\Delta V)^2 \quad (3)$$

$$P_d = \frac{E_d}{Td} 3600 \quad (4)$$

$$\eta = \frac{T_d}{Tc} \times 100 \quad (5)$$

In this study, the EIS was compared at frequency ranges of 100 mHz to 1 MHz between the CE and the WE.

RESULTS AND DISCUSSION

Thermal, Crystallographic, Spectroscopic, and Microscopic Analyses. Figure 2a shows the TG thermogram of an as-prepared Co-BTC MOF template recorded from room temperature to 800 °C. The thermogram consists of mainly two stages of weight loss for losing the different moieties shown in Table S1. The initial weight loss up to a temperature of 205 °C (stage I) is attributed to the loss of lattice water as well as DMF solvent present in the template. Literature reveals that the loss of lattice water from the templates is commonly observed up to around 150 °C, while the loss of DMF solvent is observed beyond 160 °C.[44] These two observations reveal that the first weight loss of 17.5% (stage I_a) is due to lattice water, while the remaining weight loss of around 12.93% (stage I_b) is due to the loss of DMF from the as-prepared template. Then, a stable phase of the template, where little weight change (less than 6.0%) occurs, is observed from 205 to 410 °C. Beyond 410 °C, there is a drastic second weight loss of 43.19%, which may be attributed to the loss of organic ligands of BTC of Co-BTC. Hence, the organic ligand from the template is decomposed up to 600 °C, which reveals the formation of the desired stable cobalt oxide-based composites. Furthermore, a narrow endothermic differential thermal analysis (DTA) peak at 475 °C is observed, which is consistent with an earlier report as well.[44] After 600 °C, a negligible change in the weight (1.08%) of the template is observed due to the formation of a stable CNC.

Figure 3a–d shows FESEM images of Co-BTC and the representative binary and ternary NCs. Figure 3a clearly shows

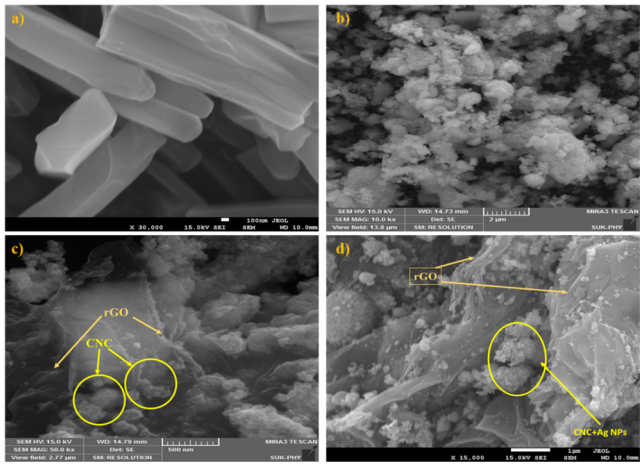

Figure 3. FESEM images of (a) Co-BTC MOF, (b) CNCAg-1.5, (c) CNCrGO-1.5, and (d) CNCAgrGO.

the Co-BTC template's square-facet nanobar morphology. FESEM images of CNC are shown in Figure S1. The highly porous grains with spherical nanoparticles are observed for binary CNCAg-1.5 in Figure 3b. Figure 3c shows porous grains on a thin sheet-like morphology for binary CNCrGO-1.5. The highly porous grains can be attributed to cobalt oxides, spherical nanoparticles to silver nanoparticles, and thin sheet-like morphology to rGO moieties. Figure 3d shows ternary composites with highly porous grains and spherical nanoparticles anchored to a thin sheet morphology. Figure 4a–c shows HRTEM images of the CNC material. The HRTEM image (Figure 4a,b) shows uniform spherical clusters of Co_3O_4@Co with an average size of 42 nm. This HRTEM image also shows uniform coatings of Co_3O_4 on Co, confirming its core–shell form. Figure 4c shows the lattice fringes of 0.194 and 0.277 nm, which correspond to the (002) plane of metallic cobalt's cubic phase and the (220) plane of cubic Co_3O_4, respectively. Additionally, this image also consists of bright white-colored fringes of CNT due to stronger chemical grafting at the Co_3O_4 and N-CNT interface.[45] The elemental mapping of CNC is shown in Figure 4d–g. The high number of carbons is beneficial for enhancing conductivity.[46]

The XRD pattern (Figure 2b) of the Co-BTC MOF template consists of the characteristic peaks at 17.5, 18.7, and 27.1° corresponding to its cubic lattices, which is consistent with previous reports.[47–49] The XRD pattern (Figure 2b) of

https://doi.org/10.1021/acsomega.2c06369
ACS Omega 2023, 8, 2183–2196

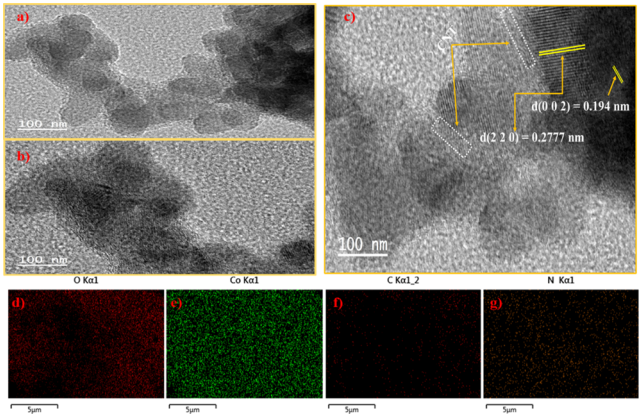

Figure 4. HRTEM images of (a,b) Co_3O_4 encapsulated in the nitrogen-doped CNT; (c) lattice fringes of Co and Co_3O_4 with unclear fringes of nitrogen-doped CNT; and (d−g) elemental mapping of CNC.

CNC consists of the characteristic peaks of elemental Co, Co_3O_4, and N-CNTs moieties. Particularly, the intense XRD peaks at 19.0, 31.2, 36.7, 59.1, and 65.3° correspond to (111), (220), (311), (511), and (440) planes, respectively, revealing the presence of cubic Co_3O_4 (#ICDD 00-043-1003) having a lattice constant value of "a" which is 8.10 Å; moreover, a characteristic peak at 44.7° corresponds to (002) of elemental Co (#ICDD 00-005-0727). In addition, a graphite XRD peak, which is in good agreement with the structure properties of CNT, is observed at 26.8°, confirming the formation of N-CNT.[40,50,51] Based on full width at half maximum, the crystallite size of Co_3O_4 is observed to be 10.15 nm in the CNC composite [calculated using peak at 2θ = 36.7° with corresponding crystal plane of (311)]. XRD patterns, with their structural information, of NF and GO and rGO are shown in Figures S2 and S3.[52]

The XRD patterns of binary $(CNC)_{1-x}(Ag\ NPs)_x$ and $(CNC)_{1-x}(rGO)_x$ NCs are shown in Figure 2c. $(CNC)_{1-x}(Ag\ NPs)_x$ patterns consist of the characteristic peaks of the individual CNC as well as elemental Ag. Among the peaks, the reflections at 38.1, 44.2, 64.4, and 77.4° correspond to (111), (200), (220), and (311), respectively, which confirms the presence of elemental Ag. Therefore, the characteristics of Bragg's reflections of both Co_3O_4@Co and elemental Ag are retained for binary $(CNC)_{1-x}(Ag\ NPs)_x$ NCs. Similarly, in the case of binary $(CNC)_{1-x}(rGO)_x$ NCs, the characteristics of the different moieties present are also retained, but the intensity of the CNC peaks decreases with rGO content. It is very advantageous to have graphitic layers present, which improves the electrical conductivity of the hybrid materials.[53]

As shown in Figure 2c, the XRD pattern of ternary CNCAgrGO composite confirms the presence of the characteristic peaks of CNC as well as Ag NPs but decrease in their intensity can be attributed to the presence of rGO.[52] The low scattering power of rGO decreases the intensity of X-ray reflections. The detailed structural cell parameters of bare, binary, as well as ternary NCs are also shown in detail in Table 1.

Figure 2d displays the FT-IR spectra of Co-BTC, CNC, CNCAg-1.5, and CNCrGO-1.5. The FT-IR spectrum of Co-BTC shows the bands at 1525 and 1430 cm^{-1}, which correspond to asymmetric (C═O) and symmetric (C−O) vibrations, respectively, of the carboxylic group in BTC. The bands at 3450 cm^{-1} (broad) as well as at 1621 cm^{-1} (sharp) are also observed, which reveal the presence of water in the metal−organic framework. In addition, the bands at 1370 and 721 cm^{-1} confirm the presence of out-of-plane (C−H) vibrations of BTC (Figure S4).[48]

The FT-IR spectrum (Figure S5) shows the bands associated with surface functional moieties of GO and rGO.[54] FT-IR spectra of CNC, CNCAg-1.5, and CNCrGO-1.5 consist of the characteristic bands at ∼1110 and ∼1380 cm^{-1} due to C−N stretching vibrations, while other bands at ∼1630, ∼2929, and 3000−3600 cm^{-1} (broad) correspond to C═C stretching vibrations, C−H stretching frequency of rGO/N-CNT and symmetric (O−H/N−H), as well as asymmetric (O−H/N−H) vibration originated from CNs (N-CNTs and RGO), respectively.[52] In addition, the FT-IR spectrum of CNC shows major bands at 500−700 cm^{-1}, indicating metal oxygen vibrational modes, while in the case of CNCAg-1.5, the peak intensity of the respective functional groups is somewhat reduced, which indicates the decrease in the amount of CNC on the surface due to the presence of Ag NPs.[55]

Raman spectroscopic studies of GO and rGO were performed and their respective patterns are seen in Figure S6.[52,56] The Raman pattern of CNC (Figure 2e) exhibits the bands at 197, 477, 520, 619, and 686 cm^{-1} corresponding to five Raman active modes (three F_{2g}, one E_g, and one A_{1g}) of the spinel phase of Co_3O_4. Figure 2f shows the D and G bands for N-CNT.[40,57,58]

Figure 5a shows the XPS survey pattern of the representative ternary CNCAgrGO materials. The survey pattern consists of the characteristic peaks due to the presence of Co-, C-, Ag-, O-, and N-species in their respective forms in the composite. The XPS spectrum of Ag 3d (Figure 5b) shows two strong peaks at 366.9 and 372.9 eV, which correspond to the binding energies of Ag $3d_{5/2}$ and Ag $3d_{3/2}$, respectively, and indicate its metallic elemental state.[59] The four major peaks in the XPS spectrum (Figure 5c) of C 1s species are observed at 284.1, 285.0, 286.5, and 288.0 eV, which are attributed to C−C, C−N, C−O, and C═O, respectively, confirming the formation of an N-doped graphitic matrix.[40,60] The XPS spectrum of Co 2p (Figure 5d) depicts the presence of metallic Co as well as its oxide. The binding energies of 778.4 and 780.6 eV are associated with Co^{3+} $2P_{3/2}$ and Co^{2+} $2P_{3/2}$, respectively, and the binding energies of 793.3 and 797.0 eV are associated with Co^{3+} $2P_{1/2}$ and Co^{2+} $2P_{1/2}$, respectively. In addition, the peak at 778.0 eV is attributed to metallic cobalt. Satellite peaks at 789.2 and 803.9 eV for Co_3O_4 were shifted to 785.5 eV and 801.9 eV for Co_3O_4@Co.[61,62]Figure 5e shows the presence of O 1s in Co_3O_4 and rGO as indicated by the binding energies of 528.4, 530.2, and 531.1 eV.[63] These energies are attributed to oxygen present in Co_3O_4, -OH functional groups on the surface, and the rest of the oxygen-containing groups in rGO, respectively. As shown in Figure 5f, binding energies of 398.1, 399.4, and 401.2 eV are ascribed to pyridine, pyrrolic, and graphitic N 1s.[64,65]

Figure 6a,b represents the BET and BJH pore volume for Co-BTC, CNC, CNCAg-1.5, CNCrGO-1.5, and CNCAgrGO. The corresponding parameters of these materials are also displayed in Table S2. The surface area of these materials is found in the range between 15.02 and 62.18 $m^2\ g^{-1}$, while pore volume is in the range between 0.017 and 0.142 $cm^3\ g^{-1}$. In addition, the average pore radius of these materials is observed between 2 to 50 nm, which confirms their mesoporous nature.

https://doi.org/10.1021/acsomega.2c06369
ACS Omega 2023, 8, 2183−2196

Table 1. Observed Structural Cell Parameters (XRD Profile) of Bare, Binary, and Ternary NCs

					cell parameters		
material	composite materials	standard d values (Å)	observed d values (Å)	(hkl) plane	a (Å)	c (Å)	V (Å^3)
CNC	Co_3O_4	2.8580	2.8688	(220)	8.1141	8.1141	534.22
		2.4374	2.4413	(311)	8.0960	8.0960	530.65
		1.5558	1.5603	(511)	8.1076	8.1076	532.93
		1.4291	1.4331	(440)	8.1068	8.1068	532.78
	Co	2.0230	2.0331	(002)	2.5029	4.0564	22.01
	N-CNT	3.3950	3.3096	(002)	2.4724	6.7088	35.83
CNCAg-1	Co_3O_4	2.8580	2.9033	(220)	8.2115	8.2115	553.69
		2.4374	2.4531	(311)	8.1363	8.1363	538.67
		1.5558	1.5551	(511)	8.0822	8.0822	527.94
		1.4291	1.4304	(440)	8.0915	8.0915	529.77
	Co	2.0230	2.0331	(002)	2.5029	4.0570	22.01
	N-CNT						
	Ag	2.3590	2.3601	(111)	4.0865	4.0865	68.24
		2.0440	2.0493	(200)	4.0975	4.0975	68.79
		1.4450	1.4444	(220)	4.0841	4.0841	68.12
		1.2310	1.2333	(311)	4.0891	4.0891	68.37
CNCAg-1.5	Co_3O_4	2.8580	2.8778	(220)	8.1394	8.1394	539.23
		2.4374	2.4416	(311)	8.0978	8.0978	531.00
		1.5558	1.5600	(511)	8.1055	8.1055	532.52
		1.4291	1.4304	(440)	8.0915	8.0915	529.76
	Co	2.0230	2.0331	(002)	2.5029	4.0570	22.01
	N-CNT						
	Ag	2.3590	2.3602	(111)	4.0865	4.0865	68.24
		2.0440	2.0479	(200)	4.0959	4.0959	68.71
		1.4450	1.4478	(220)	4.0938	4.0938	68.60
		1.2310	1.2320	(311)	4.0852	4.0852	68.17
CNCAg-2	Co_3O_4	2.8580	2.8778	(220)	8.1394	8.1394	539.23
		2.4374	2.4518	(311)	8.1314	8.1314	537.64
		1.5558	1.5653	(511)	8.1332	8.1332	538.00
		1.4291	1.4331	(440)	8.1061	8.1061	532.64
	Co	2.0230	2.0331	(002)	2.5029	4.0570	22.01
	N-CNT						
	Ag	2.3590	2.3600	(111)	4.0865	4.0865	68.24
		2.0440	2.0409	(200)	4.0816	4.0816	68.00
		1.4450	1.4498	(220)	4.0951	4.0951	68.67
		1.2310	1.2320	(311)	4.0852	4.0852	68.18
CNCrGO-1	Co_3O_4	2.8580	2.8921	(220)	8.1798	8.1798	547.30
		2.4374	2.4531	(311)	8.1352	8.1352	538.40
		1.5558	1.5639	(511)	8.1253	8.1253	536.43
		1.4291	1.4353	(440)	8.1191	8.1191	535.21
	Co	2.0230	2.0288	(002)	2.5033	4.0515	21.99
	N-CNT/rGO						
CNCrGO-1.5	Co_3O_4	2.8580	2.8743	(220)	8.1295	8.1295	537.26
		2.4374	2.4492	(311)	8.1221	8.1221	535.80
		1.5558	1.5595	(511)	8.1295	8.1295	537.26
		1.4291	1.4354	(440)	8.1092	8.1092	533.25
	Co	2.0230	2.0375	(002)	2.5025	4.0625	22.03
	N-CNT/rGO						
CNCrGO-2	Co_3O_4	2.8580	2.8706	(220)	8.1191	8.1191	535.21
		2.4374	2.4531	(311)	8.1363	8.1363	538.62
		1.5558	1.5621	(511)	8.1160	8.1160	534.59
		1.4291	1.4352	(440)	8.1191	8.1191	535.21
	Co	2.0230	2.0305	(002)	2.5032	4.0531	21.99
	N-CNT/rGO						
CNCAgrGO	Co_3O_4	2.8580	2.8921	(220)	8.1798	8.1798	547.30
		2.4374	2.4531	(311)	8.1352	8.1352	538.40
		1.5558	1.5653	(511)	8.1332	8.1332	538.00
	Co	2.0230	2.0288	(002)	2.5033	4.0515	21.99
	N-CNT/rGO						

https://doi.org/10.1021/acsomega.2c06369
ACS Omega 2023, 8, 2183−2196

Table 1. continued

material	composite materials	standard d values (Å)	observed d values (Å)	(hkl) plane	cell parameters		
					a (Å)	c (Å)	V (Å^3)
	Ag	2.3590	2.3602	(111)	4.0865	4.0865	68.24
		2.0440	2.0479	(200)	4.0959	4.0959	68.71
		1.4450	1.4478	(220)	4.0938	4.0938	68.60
		1.2310	1.2333	(311)	4.0892	4.0892	68.38

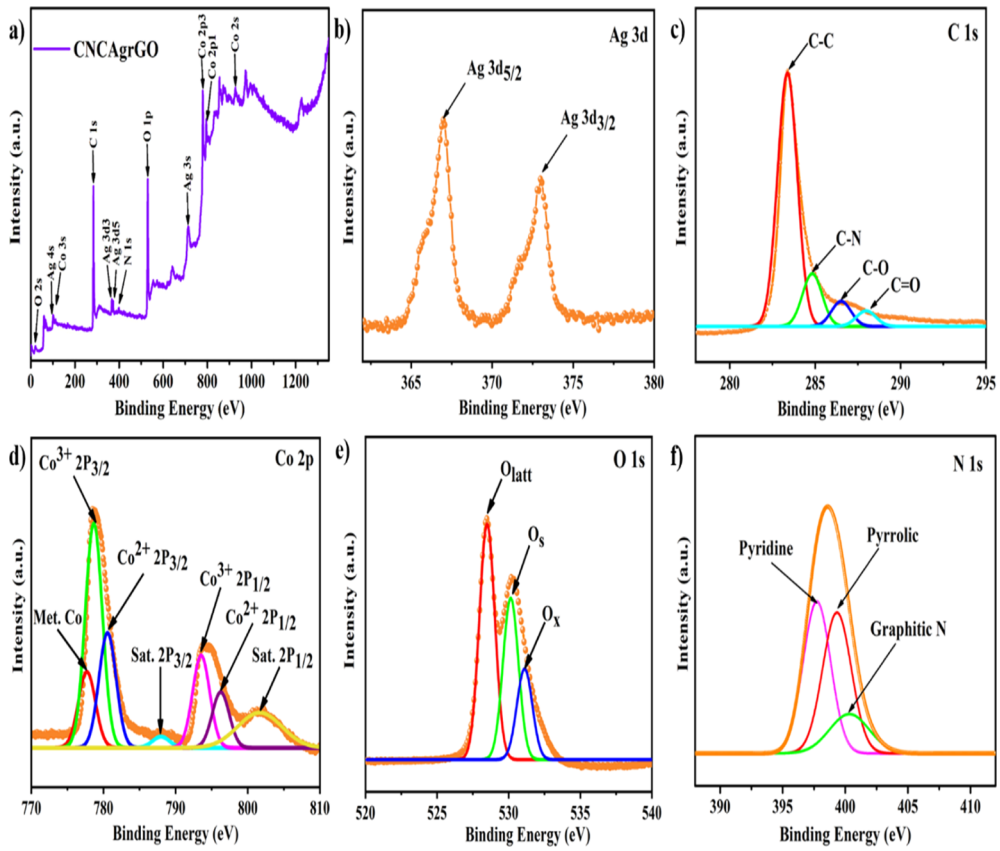

Figure 5. (a) XPS survey of CNCAgrGO, (b) Ag 3d binding energy region, (c) C 1s binding energies region, (d) Co 2p binding energy region, (e) O 1s binding energy region, and (f) N 1s binding energy region.

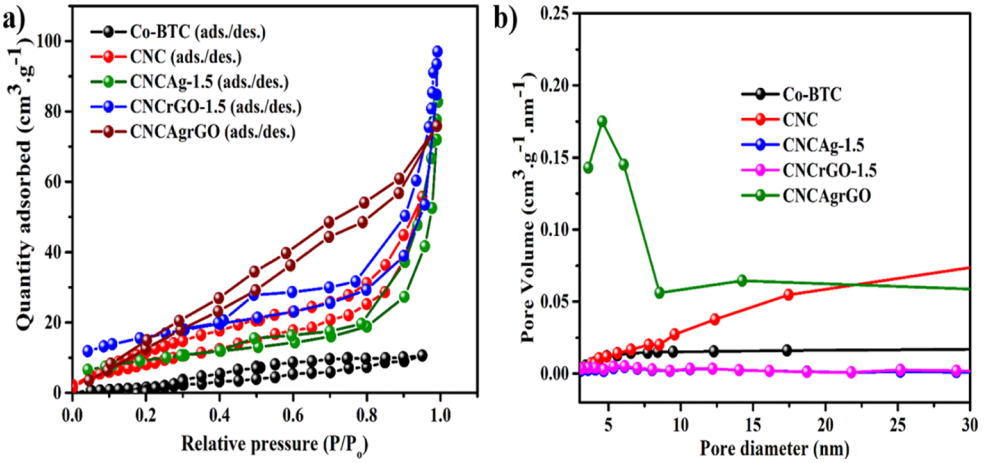

Figure 6. (a) Adsorption−desorption isotherms of Co-BTC MOF, CNC, CNCAg-1.5, CNCrGO-1.5, and CNCAgrGO. (b) BJH curves of Co-BTC MOF, CNC, CNCAg-1.5, CNCrGO-1.5, and CNCAgrGO.

It is also revealed that the surface area, pore volume, and average pore radius values of ternary composites are average as compared to those of others. Thus, the mesoporous nature of active electrode materials would provide easy infiltration due to

https://doi.org/10.1021/acsomega.2c06369
ACS Omega 2023, 8, 2183−2196

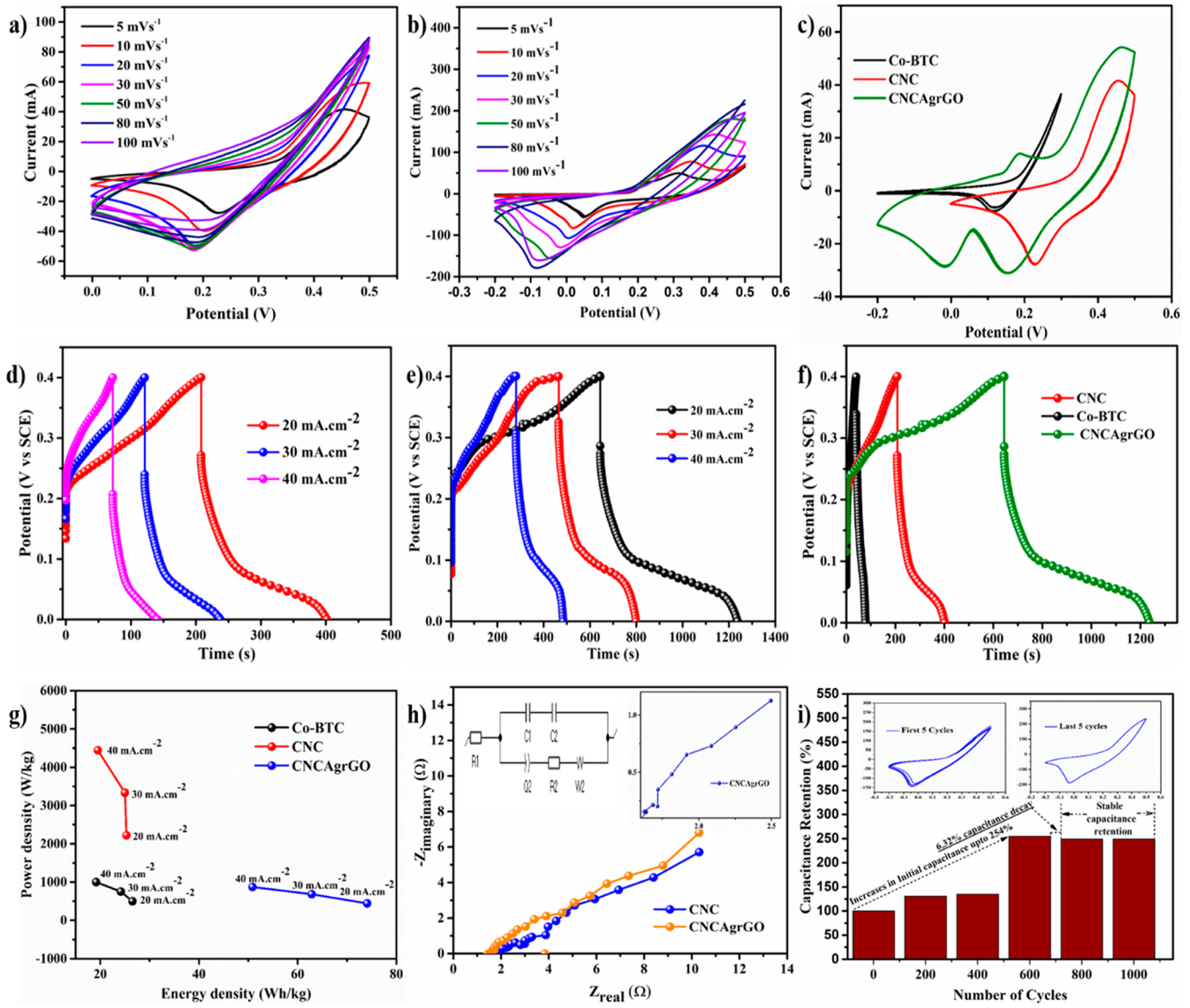

Figure 7. Electrochemical performance using a three-electrode system. (a) CV profiles of CNC at a scan rate of 5−100 mV s^{-1}, (b) CV profiles of CNCAgrGO at a scan rate of 5−100 mV s^{-1}, (C) comparative CV profiles of Co-BTC, CNC, and CNCAgrGO NC at a scan rate of 5 mV s^{-1}, (d) GCD profiles of CNC at current densities of 20−40 mA cm^{-2}, (e) GCD profiles of CNCAgrGO at current densities of 20−40 mA cm^{-2}, (f) comparative GCD profiles of Co-BTC, CNC, and CNCAgrGO NC at a current density of 20 mA cm^{-2}, (g) Ragone plots of Co-BTC, CNC, and CNCAgrGO at current densities of 20−40 mA cm^{-2}, (h) EIS studies of CNC and CNCAgrGO with insets showing an equivalent circuit and a zoomed view of EIS of CNCAgrGO, and (i) cycle stability of CNCAgrGO with insets showing first and last five cycles of 1000 continuous CV cycles.

the large pore volume, which offers more active sites for ions and electrons to transfer between the electrode surface and the electrolyte.[66] This ultimately boosts the electrochemical performance of supercapacitor devices.

Electrochemical Performance. CV studies of bare Co-BTC, CNC, binary $(CNC)_{1-x}(Ag)_x$, binary $(CNC)_{1-x}(rGO)_x$, and ternary CNCAgrGO NCs at different scan rates (from 5 to 100 mV s^{-1}) in 6 M KOH electrolyte are shown in Figures 7a,b and S7−S13. The CV profiles of all these materials consist of redox peaks, confirming pseudocapacitive behavior due to a Faradic mechanism resulting from the interaction of hydroxyl ions of KOH electrolyte with the respective electrode.[67] Redox peak intensities increase with a minor peak shift toward a higher potential as scan rates are increased, showing that quick redox reactions are happening at the interface between the active material and the electrolyte.[21] From CV plots, the specific capacitance values for bare, binary, and ternary NCs at different scan rates (5−100 mV s^{-1}) are evaluated using eq 1 and also illustrated in Tables S3−S11. CNC/NF displays a specific capacitance of 1951.1 F g^{-1} at 5 mV s^{-1}, which is higher than that of Co-BTC (509.7 F g^{-1}) at the same scan rate. In the case of binary CNCAg NCs, the specific capacitance value for representative CNCAg-1.5 (3107.1 F g^{-1}) is higher than that of the respective bare CNC (1951.1 F g^{-1}) and other binary variations. Due to the presence of noble Ag NPs, additional redox-active sites are embedded into the binary NCs, which enhances the electrochemical performance.[36] In addition, the presence of Ag NPs with metallic Co also contributes to a higher current density at higher overpotentials as metallic Co can act as a current reservoir for Co_3O_4, which lowers resistance and hence improves the conductivity of binary NCs.[68] It is also revealed that the

https://doi.org/10.1021/acsomega.2c06369
ACS Omega 2023, 8, 2183−2196

Table 2. Comparing Electrochemical Supercapacitor Performance of CNCAgrGO/NF Electrode with Previously Reported Co_3O_4-Based Electrodes

Sr.no.	material	electrolyte	specific capacitance	energy density (W h kg^{-1})	% initial capacitance retention after continuous GCD/CV cycles	refs.
1.	CoNW/CF	3 M KOH	3290.0 F g^{-1} at 5 mV s^{-1}	144.0	93.5% after 2000 GCD cycles	70
2.	PANI@Fe−Ni Co-doped Co_3O_4		1171.0 F g^{-1} at 1 A g^{-1}	6.7	84.0% after 2000 GCD cycles	71
3.	Coral-like Co_3O_4/N-CP-X	6 M KOH	316.2 F g^{-1} at 1 A g^{-1}		90.0% after 5000 GCD cycles	72
4.	3D-nanonet hollow Co_3O_4	6 M KOH	820.0 F g^{-1} at 5 mV s^{-1}	16.4	90.2% after 1000 GCD cycles	73
5.	Co_3O_4 ultrathin nanomeshes	2 M KOH	1216.4 F g^{-1} at 1 A g^{-1}	46.5		74
6.	rGO/Co_3O_4		739.0 F g^{-1} at 100 mV s^{-1}	24.7	87.5% after 5000 GCD cycles	75
7.	3D Co_3O_4/C@HCNFs	2 M KOH	1623.0 F g^{-1} at 1 A g^{-1}	36.6	85.2% after 7000 GCD cycles	76
8.	$AgCoO_2$−Co_3O_4/CMC	2 M KOH	575.0 F g^{-1} at 2 mV s^{-1}	17.0	99.0% after 5000 GCD cycles	77
9.	3D cross-network Co_3O_4−xNx	6 M KOH	666.0 F g^{-1} at 1 A g^{-1}	33.2	84.2% after 5000 GCD cycles	78
10.	Co_3O_4/rGO		800.7 F g^{-1} at 5 mV s^{-1}	31.8	80.7% after 5000 GCD cycles	79
11.	porous Co_3O_4 nanoarrays	6 M KOH	2510.0 F g^{-1} at 4 A g^{-1}	38.5	95.0% after 5000 GCD cycles	80
12.	Co_3O_4@Co_3S_4	3 M KOH	1284.0 F g^{-1} at 2 mV s^{-1}		93.1% after 5000 GCD cycles	81
13.	P-Co-MCNFs	0.1 M NaOH	821.0 F g^{-1} at 1 A g^{-1}	13.5	92.1% after 5000 GCD cycles	82
14.	Co_3O_4/N-rGO	6 M KOH	3553.0 F g^{-1} at 1 A g^{-1}	25.0	>90.0% after 3000 GCD cycles	30
15.	ultrafine Co_3O_4 nanocrystals	0.5 M H_3PO_4	1049.0 F g^{-1} at 1 mV s^{-1}	3.0		83
16.	NiO/Co_3O_4 nanocone arrays	3 M KOH	2760.0 F g^{-1} at 2 A g^{-1}	81.4	95.5% after 12,000 GCD cycles	84
17.	NiO/Co_3O_4@C/CoS_2	6 M KOH	1025.0 C g^{-1} at 1 A g^{-1}	62.8	92.0% after 5000 GCD cycles	85
18.	ZnO−Co_3O_4	3 M KOH	165.0 F g^{-1} at 2 mV s^{-1}	4.1		86
19.	$Co(OH)_2$−Co_3O_4	2 M KOH	308.0 F g^{-1} at 2 mV s^{-1}			87
20.	Co_3O_4/LIG MSCs	PVA/H_2SO_4	10.9 mF cm^{-2} at 5 mV s^{-1}	286.4 μW h cm^{-3}	97.8% after 10,000 GCD cycles	88
21.	Co_3O_4@$NiCo_2O_4$ nanoarray	1 M KOH	544.2 C g^{-1} at 1 A g^{-1}	36.0	93.0% after 5000 GCD cycles	89
22.	graphene/Co_3O_4/Polypyrrole	6 M KOH	422.0 F g^{-1} at 10 mV s^{-1}	18.4		90
23.	S-doped Co_3O_4 nanorods	2 M KOH	319.3 C g^{-1} at 0.5 A g^{-1}	38.1	87.6% after 5000 GCD cycles	91
24.	ZnO/Co_3O_4	1 M KOH	1135.0 F g^{-1} at 1 A g^{-1}	47.7	83.0% after 5000 GCD cycles	92
25.	CNCAgrGO	6 M KOH	3393.8 F g^{-1} at 5 mV s^{-1}	74.1	>93.0% after 1000 CV cycles	this work

optimum redox-active sites are present in CNCAg-1.5 for enhancing the electrochemical performance as well as electrical conductivity compared to that of other binary NCs. A similar trend is also observed for binary CNCrGO NCs where the specific capacitance is observed to be between 2000.0 and 2300.0 F g^{-1}. The electrochemical performance is higher for binary CNCrGO NCs than for bare CNCs; because of the high surface area of rGO acting as the supportive material in binary NCs, there is better intercalation−deintercalation of electrolyte ions and hence exhibits higher specific capacitance values.[27] Among both optimized binary NCs, the specific capacitance value of CNCAg-1.5 NCs is higher as compared to that of CNCrGO-1.5. Whereas Ag NPs contribute more redox sites to the electrochemical performance as compared to rGO as its capacitance contribution relies only on double-layer formation. These studies reveal that the presence of Ag NPs and rGO as supportive materials in the NCs enhances the specific capacitance as well as electrical conductivity of the host NCs. Hence, with these intentions, the ternary NCs of host CNCs with Ag NPs and rGO are explored further for electrochemical measurements.

The observed specific capacitance value for ternary CNCAgrGO NCs at 5 mV s^{-1} is 3393.8 F g^{-1}, which is almost 1.74 times greater than that of the host CNC as well as higher than other binary NCs. This also confirms the synergetic action of both supportive materials for enhancing the electrochemical performance of host CNC through the availability of more redox sites, easy infiltration, providing high surface area, and so forth. Figure 7c shows a comparative CV graph between bare and ternary NCs. The corresponding electrochemical results of these bare and NCs materials are also depicted in Table S12. All CV curves at different scan rates for ternary NCs consist of two oxidation peaks at −0.05 and 0.18 V, which are attributed to Faradaic oxidation reactions of Ag to Ag^+ and Co^{2+} to Co^{3+} in CNC, respectively, which is in good agreement with earlier reports.[55,69] In addition, the overall electrochemical performance of the ternary NCs is compared with the recent materials reported for supercapacitor studies (Table 2). The comparison reveals the efficient performance in terms of specific capacitance, energy density, stability, and so forth for ternary NCs as compared to those other reported materials.

The GCD curves of representative bare Co-BTC, CNC, binary $(CNC)_{1-x}(Ag)_x$, binary $(CNC)_{1-x}(rGO)_x$, and ternary CNCAgrGO NCs at different current densities from 20 to 40 mA cm^2 are shown in Figure 7d,e. The remaining NCs GCD curves are shown in Figures S14−S20, (ESI), and their corresponding GCD data are available in Table S13, (ESI). As per GCD studies, CNC/NF exhibits a higher specific capacitance value of 1193.7 F g^{-1} at 20 mA cm^{-2} than that at other current densities, which is also superior to that of Co-BTC. Figure 7e shows that after composting CNC with Ag NPs and rGO, GCD lines have less symmetry in charging−discharging cycle time; in particular, CNCrGO-1.5 (Figure S16, ESI) and CNCAg-1.5 (Figure S19, ESI) NCs have a longer charge−discharge time than their respective binary variations.[93]Figure 7f shows comparative GCD plots of the bare Co-BTC, CNC, and ternary CNCAgrGO NCs in 6 M KOH at a current density of 20 mA cm^{-2}. The synergistic effect of the composite materials in the ternary NCs is responsible for the amplified electrochemical performance compared to that of the binary and other bare materials. The ternary CNCAgrGO/NF in the 6 M KOH electrolyte exhibited an excellent specific capacitance value of 3333.5 F

https://doi.org/10.1021/acsomega.2c06369
ACS Omega 2023, 8, 2183−2196

g^{-1}, calculated using eq 2 at a current density of 20 mA cm^{-2}. As shown in Table S13, (ESI), bare and NC materials showed different specific capacitance values as a function of current density. In most cases, the specific capacitance results observed from GCD for the CNCAgrGO NC and CNC profiles agree substantially with the CV results. Furthermore, the discharge time for the CNCAgrGO NC is longer than for other bare and binary NCs materials. By comparing the GCD curves of all materials, it is evident that all materials exhibit the ideal capacitive behavior. As current density increases, specific capacitance values decrease; just as in CV studies, as scan rate increases, specific capacitance values decrease and vice-versa.

Figure 7g depicts the power density and energy density of representative ternary NCs and bare materials. The electrochemical parameters such as energy density, power density, and coulombic efficiency of the electrodes are assessed from GCD profiles using eqs 3−5 at different current densities and are also illustrated in Table S13, (ESI). All bare, binary, and ternary NCs demonstrate good coulombic efficiency. At 20 mA cm^{-2}, the power density for CNC and CNCAgrGO NC is 500.0 and 443.3 W Kg^{-1}, respectively. As observed from the calculated values of GCD curves, the power density increases with increasing current density, but the energy density has an inverse relationship with current density. At 20 mA cm^{-2}, the energy density was found to be 26.5 and 74.1 W h Kg^{-1} for CNC and CNCAgrGO NCs, respectively, which decreased to 19.2 and 50.8 W h Kg^{-1} at 40 mA cm^{-2}. At a current density of 20 mA cm^{-2}, the observed energy density trend for the electrodes is CNCAgrGO > CNCAg-1.5 > CNCrGO-1.5 > CNC > Co-BTC, while the reverse trend is noted in the power density value for all these materials. The excellent energy density of ternary CNCAgrGO is supported by noble metals and Co with reserved electrons.

Furthermore, EIS is used to assess charge-transfer resistance and series resistance of representative bare and ternary NCs (Figure 7h). Based on an EIS equivalent circuit, the Nyquist plot of the ternary CNCAgrGO material is shown in the inset of Figure 7h. While the Nyquist plots of the remaining NCs are shown in Figure S21, (ESI).[69] The Nyquist plots in Table 3

Table 3. EIS Parameters for CNCAgrGO/NF in 6 M KOH Electrolyte

	EIS parameters	
materials	R_s (Ω)	R_{ct} (Ω)
CNC	3.01	0.88
CNCrGO-1.5	1.99	0.80
CNCAg-1.5	0.66	0.03
CNCAgrGO	1.70	0.15

show that ternary NCs have lower R_s (1.705 Ω) and R_{ct} (0.15 Ω) values than bare NCs. This is attributed to the electrical conductivity of Ag NPs as well as the ballistic conductivity of RGO.[28,36]

In addition, along with having excellent specific capacitance values, the stability of the active electrode material also plays a vital role in electrochemical performance. To test the stability, ternary CNCAgrGO/NF was subjected to 1000 CV cycles, as shown in Figure 7i. In the first 600 cycles, the electrode material is observed to be undergoing activation, and after full activation of the material, a 6.32% decay in capacitance values is observed between 600 and 720 cycles. Furthermore, beyond 720 cycles, stable capacitance retention is observed from continuous CV cycles of CNCAgrGO electrode materials. Based on these performances, ternary CNCAgrGO NCs exhibit excellent rate capability, specific capacitance, and cycle stability, and hence these NCs are explored further for fabricating asymmetric supercapacitor devices.

Asymmetric Supercapacitors Device. Figure 8a−c depicts the electrode deposition, device fabrication with CNCAgrGO/NF as the cathode and activated carbon/NF as the anode electrode, and a schematic of the fabricated device. In the present device testing, a potential window was optimized to 1.7 V, where the cell voltage was calculated as the sum of the potential ranges of the two electrodes, viz., −0.2 to 0.5 V from CNCAgrGO and −1.0 to 0.0 V from activated carbon as shown in Figure 8d. All of the CV profiles in Figure 8e at various scan rates (up to 100 mV s^{-1}) exhibit non-rectangular characteristics, revealing the Faradaic mechanism of CNC NCs.[94] It also shows excellent and ideal supercapacitor performance in a potential window of 1.7 V. Using CV curves, the specific capacitance value of the aqueous asymmetric supercapacitor is observed to be 413.8 F g^{-1} at a scan rate of 5 mV s^{-1} as well as 35.5 F g^{-1} at a scan rate of 100 mV s^{-1}, which is also shown in Table S14, (ESI). Figure 8f depicts GCD curves at different current densities ranging from 20 to 50 mA cm^{-2}. According to evaluated results illustrated in Table S15, (ESI), a power density of 5000.0 W kg^{-1} and an energy density of 4.9 W h kg^{-1} are noted for CNCAgrGO/NF//activated carbon/NF. The obtained results of this device are superior to those obtained with the previous reported devices. It has been demonstrated that the device is stable when subjected to 1000 continuous CV cycles, as shown in Figure 8h. The complete activation of the material is observed for up to an initial 400 continuous cycles. Thereafter, no decay in capacitance is observed, that is, stable cycles are observed. Figure 8h (inset) shows the activation and retention of the same CV curve for 1−500 and 500−1000 continuous cycles. Based on electrochemical impedance measurements, Figure 8g illustrates a lower charge-transfer resistance (R_{ct} = ∼0.0186 Ω) for the device. Figure 8g shows an inset of an equivalent circuit for the device.

CONCLUSIONS

Co-BTC nanobars were synthesized solvothermally under alkaline conditions in the current study, and these nanobars were then used to form host CNC NCs. The stoichiometry of porous CNC NCs with Ag NPs, as well as rGO, was optimized in order to obtain ternary NCs with excellent supercapacitor performance. The evaluated specific capacitance values for the host CNCs and optimized ternary CNCAgrGO NCs at 5 mV s^{-1} were 1951.2 and 3393.8 F g^{-1}, respectively. In addition, ternary CNCAgrGO NCs exhibited good cycle stability up to 1000 cycles, having the energy and power density values of 74.1 W kg^{-1} and 443.7 W h kg^{-1}, respectively. The enhanced electrochemical results can be attributed to the proper intercalation−de-intercalation of electrolyte ions, more redox-active sites, and the chemical stability of materials. The present ternary NC-based aqueous asymmetric supercapacitor device (CNCAgrGO/NF//activated carbon/NF) showed an excellent energy density of 4.9 W h kg^{-1} at a power density of 5000.0 W kg^{-1}. Also, when subjected to continuous CV cycles at the scan rate of 100 mV s^{-1}, an overlap of CV curves of 500 and 1000 cycles was observed, illustrating the stability of the device. Thus, the present strategy provides a convenient and

https://doi.org/10.1021/acsomega.2c06369
ACS Omega 2023, 8, 2183−2196

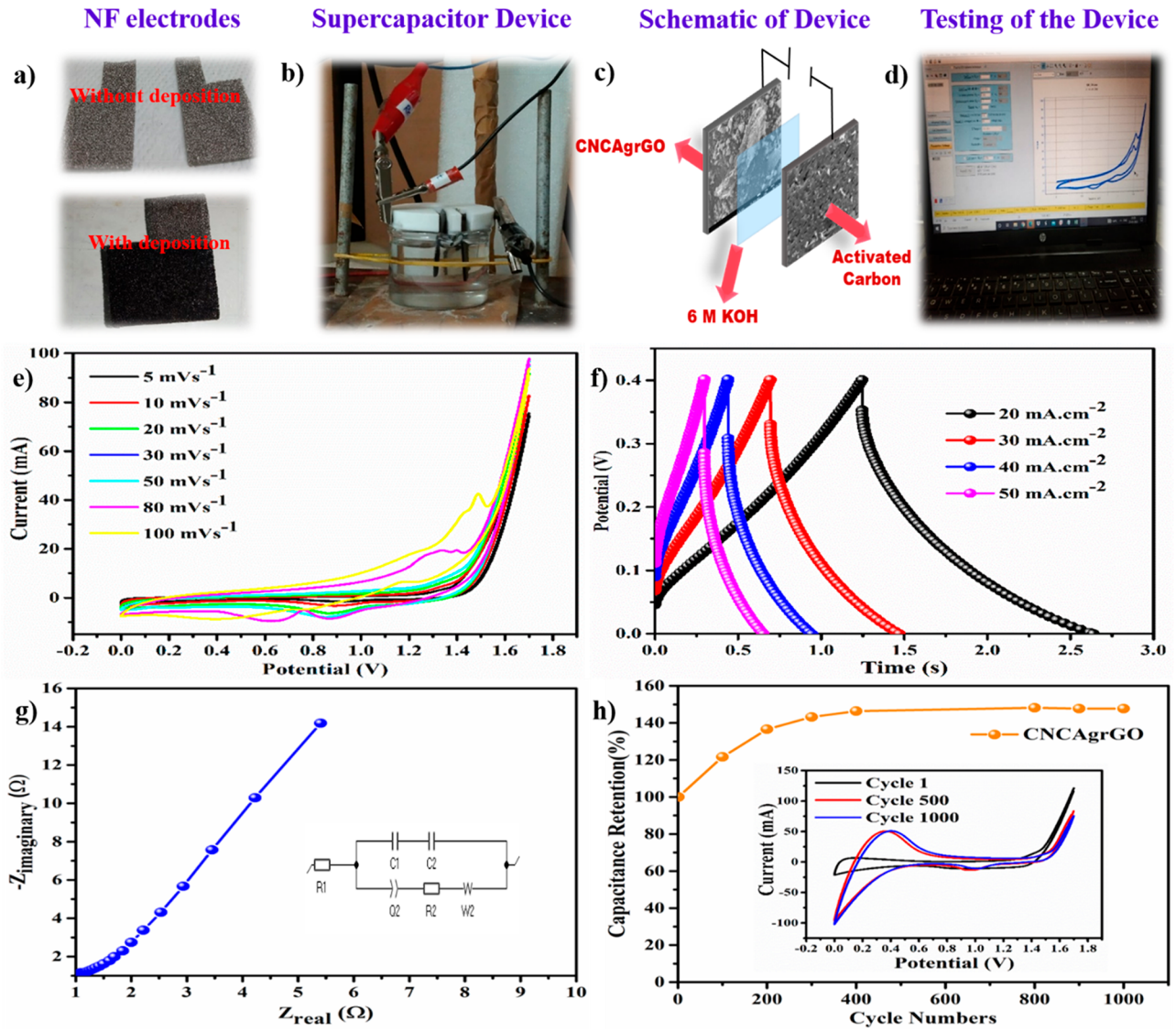

Figure 8. (a) Before and after deposition on current collectors; (b) aqueous asymmetric supercapacitor device; (c) schematic illustration of the device; (d) optimization of the operating window for the device; (e) CV study of the device at a scan rate of 5−100 mV s^{-1}; (f) GCD study of the device at current densities of 20−40 mA cm^{-2}; (g) EIS study of the device with inset showing the equivalent circuit; and (h) stability of the device with inset showing comparison with respect to CV cycle number 1, 500, and 1000 of 1000 continuous CV cycles.

easiest way for synthesizing efficient and high-performing electrode materials for energy storage applications.

■ ASSOCIATED CONTENT

Supporting Information

The Supporting Information is available free of charge at https://pubs.acs.org/doi/10.1021/acsomega.2c06369.

Materials and synthesis of GO and rGO; TGA, FESEM, XRD, FTIR, Raman, BET, and CV analyses; comparison of bare, binary, and ternary protocols; galvanostatic charge−discharge studies; and specific capacitance and energy density values for asymmetric aqueous supercapacitor device at different scan rates (PDF)

■ AUTHOR INFORMATION

Corresponding Author

Sagar D. Delekar − *Department of Chemistry, Shivaji University, Kolhapur 416 004 Maharashtra, India;* orcid.org/0000-0002-4510-305X; Phone: +91-231-2609311; Email: sddelekar7@rediffmail.com, sdd_chem@unishivaji.ac.in; Fax: +91-231-2692333

Authors

Swapnajit V. Mulik − *Department of Chemistry, Shivaji University, Kolhapur 416 004 Maharashtra, India*

Suprimkumar D. Dhas − *Thin Film Nanomaterial, Department of Physics, Shivaji University, Kolhapur 416 004 Maharashtra, India*

Annasaheb V. Moholkar − *Thin Film Nanomaterial, Department of Physics, Shivaji University, Kolhapur 416 004 Maharashtra, India*

Vinayak G. Parale − *Department of Materials Science and Engineering, Yonsei University, Seoul 03722, South Korea*

Hyung-Ho Park − *Department of Materials Science and Engineering, Yonsei University, Seoul 03722, South Korea;* orcid.org/0000-0001-5540-5433

Pramod A. Koyale − *Department of Chemistry, Shivaji University, Kolhapur 416 004 Maharashtra, India*

https://doi.org/10.1021/acsomega.2c06369
ACS Omega 2023, 8, 2183−2196

Vijay S. Ghodake − *Department of Chemistry, Shivaji University, Kolhapur 416 004 Maharashtra, India*
Dillip K. Panda − *Department of Materials Science and Engineering, Clemson University, Clemson, South Carolina 29631, United States*

Complete contact information is available at: https://pubs.acs.org/10.1021/acsomega.2c06369

Author Contributions

Experimental work was designed by S.V.M. and S.D.D. All synthesis parts have been completed by S.V.M. Electrochemical tests were conducted by S.V.M., S.D., and A.V.M. Some characterizations were carried out by V.G.P. and H.-H.P. Studies on whole supercapacitors were conducted by S.V.M. and S.D.D. S.V.M., S.D.D., and D.K.P. analyzed the data and wrote the entire manuscript. P.A.K. and other co-authors reviewed the manuscript.

Notes

The authors declare no competing financial interest.

■ ACKNOWLEDGMENTS

The author S.V.M. gratefully acknowledges Chhatrapati Shahu Maharaj Research, Training and Human Development Institute (SARTHI), Pune [CSMNRF-2021 (CSMNRF-2021/2021-22/896)].

■ REFERENCES

(1) Panda, P. K.; Grigoriev, A.; Mishra, Y. K.; Ahuja, R. Progress in Supercapacitors: Roles of Two Dimensional Nanotubular Materials. *Nanoscale Adv.* **2020**, *2*, 70−108.
(2) Vlad, A.; Singh, N.; Rolland, J.; Melinte, S.; Ajayan, P. M.; Gohy, J. F. Hybrid Supercapacitor-Battery Materials for Fast Electrochemical Charge Storage. *Sci. Rep.* **2014**, *4*, 1−7.
(3) Mulik, S. V.; Jadhav, S. A.; Patil, P. S.; Delekar, S. D.4-Transition Metal Oxide−Conducting Polymer Nanocomposites and Metal-Organic Framework-Based Composites for Supercapacitor Application. *Advances in Metal Oxides and Their Composites for Emerging Applications*; Elsevier, 2022; pp 135−185.
(4) Ren, Z.; Li, J.; Ren, Y.; Wang, S.; Qiu, Y.; Yu, J. Large-Scale Synthesis of Hybrid Metal Oxides through Metal Redox Mechanism for High-Performance Pseudocapacitors. *Sci. Rep.* **2016**, *6*, 1−10.
(5) An, C.; Zhang, Y.; Guo, H.; Wang, Y. Metal Oxide-Based Supercapacitors: Progress and Prospectives. *Nanoscale Adv.* **2019**, *1*, 4644−4658.
(6) Wang, G.; Zhang, L.; Zhang, J. A Review of Electrode Materials for Electrochemical Supercapacitors. *Chem. Soc. Rev.* **2012**, *41*, 797−828.
(7) Yu, G.; Hu, L.; Liu, N.; Wang, H.; Vosgueritchian, M.; Yang, Y.; Cui, Y.; Bao, Z. Enhancing the Supercapacitor Performance of Graphene/MnO_2 Nanostructured Electrodes by Conductive Wrapping. *Nano Lett.* **2011**, *11*, 4438−4442.
(8) Lu, Q.; Chen, J. G.; Xiao, J. Q. Nanostructured Electrodes for High-Performance Pseudocapacitors. *Angew. Chem., Int. Ed.* **2013**, *52*, 1882−1889.
(9) Sharma, V.; Singh, I.; Chandra, A. Hollow Nanostructures of Metal Oxides as next Generation Electrode Materials for Supercapacitors. *Sci. Rep.* **2018**, *8*, 1−12.
(10) Ye, J.; Li, Z.; Dai, Z.; Zhang, Z.; Guo, M.; Wang, X. Facile Synthesis of Hierarchical CuO Nanoflower for Supercapacitor Electrodes. *J. Electron. Mater.* **2016**, *45*, 4237−4245.
(11) Wang, B. R.; Hu, Y.; Pan, Z.; Wang, J. MOF-Derived Manganese Oxide/Carbon Nanocomposites with Raised Capacitance for Stable Asymmetric Supercapacitor. *RSC Adv.* **2020**, *10*, 34403−34412.
(12) Salunkhe, R. R.; Kaneti, Y. V.; Yamauchi, Y. Metal-Organic Framework-Derived Nanoporous Metal Oxides toward Supercapacitor Applications: Progress and Prospects. *ACS Nano* **2017**, *11*, 5293−5308.
(13) Zhang, X.; Tian, X.; Liu, C.; Qiao, J.; Liu, W.; Liu, J.; Zeng, Z. MnCo-MOF-74 Derived Porous MnO/Co/C Heterogeneous Nanocomposites for High-Efficiency Electromagnetic Wave Absorption. *Carbon* **2022**, *194*, 257−266.
(14) Tian, H.; Qiao, J.; Yang, Y.; Xu, D.; Meng, X.; Liu, W.; Zhang, X.; Li, B.; Wu, L.; Zeng, Z.; Liu, J. ZIF-67-Derived Co/C Embedded Boron Carbonitride Nanotubes for Efficient Electromagnetic Wave Absorption. *Chem. Eng. J.* **2022**, *450*, 138011.
(15) Tan, X.; Wu, Y.; Lin, X.; Zeb, A.; Xu, X.; Luo, Y.; Liu, J. Application of MOF-Derived Transition Metal Oxides and Composites as Anodes for Lithium-Ion Batteries. *Inorg. Chem. Front.* **2020**, *7*, 4939−4955.
(16) Wang, J.; Zhang, Y.; Ye, J.; Wei, H.; Hao, J.; Mu, J.; Zhao, S.; Hussain, S. Facile Synthesis of Three-Dimensional $NiCo_2O_4$ with Different Morphology for Supercapacitors. *RSC Adv.* **2016**, *6*, 70077−70084.
(17) Aljaafari, A.; Parveen, N.; Ahmad, F.; Alam, M. W.; Ansari, S. A. Self-Assembled Cube-like Copper Oxide Derived from a Metal-Organic Framework as a High-Performance Electrochemical Supercapacitive Electrode Material. *Sci. Rep.* **2019**, *9*, 1−10.
(18) Salunkhe, R. R.; Tang, J.; Kamachi, Y.; Nakato, T.; Kim, J. H.; Yamauchi, Y. Asymmetric Supercapacitors Using 3D Nanoporous Carbon and Cobalt Oxide Electrodes Synthesized from a Single Metal-Organic Framework. *ACS Nano* **2015**, *9*, 6288−6296.
(19) Han, Y.; Zhang, S.; Shen, N.; Li, D.; Li, X. MOF-Derived Porous NiO Nanoparticle Architecture for High Performance Supercapacitors. *Mater. Lett.* **2017**, *188*, 1−4.
(20) Dai, E.; Xu, J.; Qiu, J.; Liu, S.; Chen, P.; Liu, Y. Co@Carbon and Co_3O_4@Carbon Nanocomposites Derived from a Single MOF for Supercapacitors. *Sci. Rep.* **2017**, *7*, 1−11.
(21) Numan, A.; Duraisamy, N.; Saiha Omar, F.; Mahipal, Y. K.; Ramesh, K.; Ramesh, S. Enhanced Electrochemical Performance of Cobalt Oxide Nanocube Intercalated Reduced Graphene Oxide for Supercapacitor Application. *RSC Adv.* **2016**, *6*, 34894−34902.
(22) Adarsh, N. N.Metal−Organic Framework (MOF)−Derived Metal Oxides for Supercapacitors. In *Metal Oxides, Metal Oxides in Supercapacitors*; Dubal, D. P., Gomez-Romero, P., Eds.; Elsevier, 2017; pp 165−192. https://doi.org/10.1016/B978-0-12-810464-4.00007-3
(23) Vilian, A. T. E.; Dinesh, B.; Rethinasabapathy, M.; Hwang, S. K.; Jin, C. S.; Huh, Y. S.; Han, Y. K. Hexagonal Co_3O_4 Anchored Reduced Graphene Oxide Sheets for High-Performance Supercapacitors and Non-Enzymatic Glucose Sensing. *J. Mater. Chem. A* **2018**, *6*, 14367−14379.
(24) Ji, Y.; Ma, Y.; Liu, R.; Ma, Y.; Cao, K.; Kaiser, U.; Varzi, A.; Song, Y. F.; Passerini, S.; Streb, C. Modular Development of Metal Oxide/Carbon Composites for Electrochemical Energy Conversion and Storage. *J. Mater. Chem. A* **2019**, *7*, 13096−13102.
(25) Kaipannan, S.; Govindarajan, K.; Sundaramoorthy, S.; Marappan, S. Waste Toner-Derived Carbon/Fe_3O_4 Nanocomposite for High-Performance Supercapacitor. *ACS Omega* **2019**, *4*, 15798−15805.
(26) Veerakumar, P.; Sangili, A.; Manavalan, S.; Thanasekaran, P.; Lin, K. C. Research Progress on Porous Carbon Supported Metal/Metal Oxide Nanomaterials for Supercapacitor Electrode Applications. *Ind. Eng. Chem. Res.* **2020**, *59*, 6347−6374.
(27) Umeshbabu, E.; Rajeshkhanna, G.; Justin, P.; Rao, G. Synthesis of Mesoporous $NiCo_2O_4$-RGO by a Solvothermal Method for Charge Storage Applications. *RSC Adv.* **2015**, *5*, 66657−66666.
(28) Mohan, V. B.; Brown, R.; Jayaraman, K.; Bhattacharyya, D. Characterisation of Reduced Graphene Oxide: Effects of Reduction Variables on Electrical Conductivity. *Mater. Sci. Eng., B* **2015**, *193*, 49−60.
(29) Shafi, P. M.; Ganesh, V.; Bose, A. C. $LaMnO_3$/RGO/PANI Ternary Nanocomposites for Supercapacitor Electrode Application and Their Outstanding Performance in All-Solid-State Asymmetrical Device Design. *ACS Appl. Energy Mater.* **2018**, *1*, 2802−2812.

(30) Tian, X.; Sun, X.; Jiang, Z.; Jiang, Z. J.; Hao, X.; Shao, D.; Maiyalagan, T. Exploration of the Active Center Structure of Nitrogen-Doped Graphene for Control over the Growth of Co_3O_4 for a High-Performance Supercapacitor. *ACS Appl. Energy Mater.* **2018**, *1*, 143−153.
(31) Ghosh, D.; Lim, J.; Narayan, R.; Kim, S. O. High Energy Density All Solid State Asymmetric Pseudocapacitors Based on Free Standing Reduced Graphene Oxide-Co_3O_4 Composite Aerogel Electrodes. *ACS Appl. Mater. Interfaces* **2016**, *8*, 22253−22260.
(32) Xu, J.; Zhang, W.; Chen, Y.; Fan, H.; Su, D.; Wang, G. MOF-Derived Porous N−Co_3O_4@N−C Nanododecahedra Wrapped with Reduced Graphene Oxide as a High Capacity Cathode for Lithium−Sulfur Batteries. *J. Mater. Chem. A* **2018**, *6*, 2797−2807.
(33) Sawangphruk, M.; Suksomboon, M.; Kongsupornsak, K.; Khuntilo, J.; Srimuk, P.; Sanguansak, Y.; Klunbud, P.; Suktha, P.; Chiochan, P. High-Performance Supercapacitors Based on Silver Nanoparticle-Polyaniline- Graphene Nanocomposites Coated on Flexible Carbon Fiber Paper. *J. Mater. Chem. A* **2013**, *1*, 9630−9636.
(34) Zheng, S.; Li, Q.; Xue, H.; Pang, H.; Xu, Q. A Highly Alkaline-Stable Metal Oxide@metal-Organic Framework Composite for High-Performance Electrochemical Energy Storage. *Natl. Sci. Rev.* **2020**, *7*, 305−314.
(35) Yan, Y.; Wang, T.; Li, X.; Pang, H.; Xue, H. Noble metal-based materials in high-performance supercapacitors. *Inorg. Chem. Front.* **2017**, *4*, 33−51.
(36) Maheswari, N.; Muralidharan, G. Ag-Incorporated CeO2 Nano Cauliflowers for High-Performance Supercapacitor Devices. *New J. Chem.* **2017**, *41*, 10841−10850.
(37) Çıplak, C.; Yıldız, Y. The effect of Ag loading on supercapacitor performance of graphene based nanocomposites. *Fullerenes, Nanotubes, Carbon Nanostruct.* **2019**, *27*, 65−76.
(38) Yoon, Y.; Samanta, K.; Lee, H.; Lee, K.; Tiwari, A. P.; Lee, J.; Yang, J.; Lee, H. Highly Stretchable and Conductive Silver Nanoparticle Embedded Graphene Flake Electrode Prepared by In Situ Dual Reduction Reaction. *Sci. Rep.* **2015**, *5*, 1−10.
(39) Shahriary, L.; Nair, R.; Sabharwal, S.; Athawale, A. A. One-Step Synthesis of Ag-Reduced Graphene Oxide-Multiwalled Carbon Nanotubes for Enhanced Antibacterial Activities. *New J. Chem.* **2015**, *39*, 4583−4590.
(40) Singh, T.; Das, C.; Bothra, N.; Sikdar, N.; Das, S.; Pati, S. K.; Maji, T. K. MOF Derived Co_3O_4@Co/NCNT Nanocomposite for Electrochemical Hydrogen Evolution, Flexible Zinc-Air Batteries, and Overall Water Splitting. *Inorg. Chem.* **2020**, *59*, 3160−3170.
(41) Li, X.; Zhang, J.; Xu, W.; Jia, H.; Wang, X.; Yang, B.; Zhao, B.; Li, B.; Ozaki, Y. Mercaptoacetic Acid-Capped Silver Nanoparticles Colloid: Formation, Morphology, and SERS Activity. *Langmuir* **2003**, *19*, 4285−4290.
(42) Saraf, M.; Rajak, R.; Mobin, S. M. A Fascinating Multitasking Cu-MOF/RGO Hybrid for High Performance Supercapacitors and Highly Sensitive and Selective Electrochemical Nitrite Sensors. *J. Mater. Chem. A* **2016**, *4*, 16432−16445.
(43) Deshmukh, S. P.; Mullani, S. B.; Koli, V. B.; Patil, S. M.; Kasabe, P. J.; Dandge, P. B.; Pawar, S. A.; Delekar, S. D. Ag Nanoparticles Connected to the Surface of TiO_2 Electrostatically for Antibacterial Photoinactivation Studies. *Photochem. Photobiol.* **2018**, *94*, 1249−1262.
(44) Chen, D.; Chen, S.; Jiang, Y.; Xie, S.; Quan, H.; Hua, L.; Luo, X.; Guo, L. Heterogeneous Fenton-like Catalysis of Fe-MOF Derived Magnetic Carbon Nanocomposites for Degradation of 4-Nitrophenol. *RSC Adv.* **2017**, *7*, 49024−49030.
(45) Delekar, S. D.; Dhodamani, A. G.; More, K. V.; Dongale, T. D.; Kamat, R. K.; Acquah, S. F. A.; Dalal, N. S.; Panda, D. K. Structural and Optical Properties of Nanocrystalline TiO2 with Multiwalled Carbon Nanotubes and Its Photovoltaic Studies Using Ru(II) Sensitizers. *ACS Omega* **2018**, *3*, 2743.
(46) Sevilla, M.; Fuertes, A. B. Catalytic Graphitization of Templated Mesoporous Carbons. *Carbon* **2006**, *44*, 468−474.
(47) Yaghi, O. M.; Li, H.; Groy, T. L. Construction of Porous Solids from Hydrogen-Bonded Metal Complexes of 1,3,5-Benzenetricarboxylic Acid. *J. Am. Chem. Soc.* **1996**, *118*, 9096−9101.
(48) Yang, N.; Song, H.; Wan, X.; Fan, X.; Su, Y.; Lv, Y. A Metal (Co)-Organic Framework-Based Chemiluminescence System for Selective Detection of l-Cysteine. *Analyst* **2015**, *140*, 2656−2663.
(49) Punde, N. S.; Rawool, C. R.; Rajpurohit, A. S.; Karna, S. P.; Srivastava, A. K. Hybrid Composite Based on Porous Cobalt-Benzenetricarboxylic Acid Metal Organic Framework and Graphene Nanosheets as High Performance Supercapacitor Electrode. *ChemistrySelect* **2018**, *3*, 11368−11380.
(50) Fu, S.; Zhu, C.; Li, H.; Du, D.; Lin, Y. One-Step Synthesis of Cobalt and Nitrogen Co-Doped Carbon Nanotubes and Their Catalytic Activity for the Oxygen Reduction Reaction. *J. Mater. Chem. A* **2015**, *3*, 12718−12722.
(51) Xia, Y.; Mokaya, R. Generalized and Facile Synthesis Approach to N-Doped Highly Graphitic Mesoporous Carbon Materials. *Chem. Mater.* **2005**, *17*, 1553−1560.
(52) Mullani, S. B.; Dhodamani, A. G.; Shellikeri, A.; Mullani, N. B.; Tawade, A. K.; Tayade, S. N.; Biscay, J.; Dennany, L.; Delekar, S. D. Structural Refinement and Electrochemical Properties of One Dimensional $(ZnO\ NRs)_{1-x}(CNs)_x$ Functional Hybrids for Serotonin Sensing Studies. *Sci. Rep.* **2020**, *10*, 1−18.
(53) Young, C.; Kim, J.; Kaneti, Y. V.; Yamauchi, Y. One-Step Synthetic Strategy of Hybrid Materials from Bimetallic Metal−Organic Frameworks for Supercapacitor Applications. *ACS Appl. Energy Mater.* **2018**, *1*, 2007−2015.
(54) Du, F. P.; Cao, N. N.; Zhang, Y. F.; Fu, P.; Wu, Y. G.; Lin, Z. D.; Shi, R.; Amini, A.; Cheng, C. PEDOT:PSS/Graphene Quantum Dots Films with Enhanced Thermoelectric Properties via Strong Interfacial Interaction and Phase Separation. *Sci. Rep.* **2018**, *8*, 1−12.
(55) Ashok, A.; Kumar, A.; Matin, M. A.; Tarlochan, F. Synthesis of Highly Efficient Bifunctional Ag/Co_3O_4 Catalyst for Oxygen Reduction and Oxygen Evolution Reactions in Alkaline Medium. *ACS Omega* **2018**, *3*, 7745−7756.
(56) Dhodamani, A. G.; More, K. V.; Koli, V. B.; Shelke, A. R.; Deshpande, N. G.; Panda, D. K.; Delekar, S. D. Compositional Dependent Physicochemical and Photovoltaic Properties of the $(TiO_2)_{1-x}(RGO)_x$ Nanocomposites for Sensitized Solar Cells Using Ru(II) Dyes. *ChemistrySelect* **2019**, *4*, 1055−1068.
(57) Zhao, Y.; Chen, S.; Sun, B.; Su, D.; Huang, X.; Liu, H.; Yan, Y.; Sun, K.; Wang, G. Graphene-Co_3O_4 Nanocomposite as Electrocatalyst with High Performance for Oxygen Evolution Reaction. *Sci. Rep.* **2015**, *5*, 7629.
(58) Shen, Q.; Yang, J.; Chen, K. L.; Wang, H.; Liu, J. B.; Yan, H. Co_3O_4 Nanorods−Graphene Composites as Catalysts for Rechargeable Zinc-Air Battery. *J. Solid State Electrochem.* **2016**, *20*, 3331−3336.
(59) Xue, M.; Liu, S.; Guo, J.; Guo, Q. Growth and Electronic Structure of Ag on Polar MgO(111) Films. *RSC Adv.* **2013**, *3*, 18916−18922.
(60) Sikdar, N.; Konkena, B.; Masa, J.; Schuhmann, W.; Maji, T. Co_3O_4@Co/NCNT Nanostructure Derived from a Dicyanamide-Based Metal-Organic Framework as an Efficient Bi-functional Electrocatalyst for Oxygen Reduction and Evolution Reactions. *Chem. - Eur. J.* **2017**, *23*, 18049−18056.
(61) Alex, C.; Sarma, S. C.; Peter, S. C.; John, N. S. Competing Effect of Co^{3+} Reducibility and Oxygen-Deficient Defects Toward High Oxygen Evolution Activity in Co_3O_4 Systems in Alkaline Medium. *ACS Appl. Energy Mater.* **2020**, *3*, 5439−5447.
(62) Gao, Y.; Mi, L.; Wei, W.; Cui, S.; Zheng, Z.; Hou, H.; Chen, W. Double Metal Ions Synergistic Effect in Hierarchical Multiple Sulfide Microflowers for Enhanced Supercapacitor Performance. *ACS Appl. Mater. Interfaces* **2015**, *7*, 4311−4319.
(63) Kooti, M.; Sedeh, A. N.; Gheisari, K.; Figuerola, A. Synthesis, Characterization, and Performance of Nanocomposites Containing Reduced Graphene Oxide, Polyaniline, and Cobalt Ferrite. *Phys. B* **2021**, *612*, 412974.
(64) Sarkar, B.; Barman, B. K.; Nanda, K. K. Non-Precious Bimetallic CoCr Nanostructures Entrapped in Bamboo-Like Nitro-

https://doi.org/10.1021/acsomega.2c06369
ACS Omega 2023, 8, 2183−2196

gen-Doped Graphene Tube As a Robust Bifunctional Electrocatalyst for Total Water Splitting. *ACS Appl. Energy Mater.* **2018**, *1*, 1116−1126.
(65) Zhang, T.; He, C.; Sun, F.; Ding, Y.; Wang, M.; Peng, L.; Wang, J.; Lin, Y. Co_3O_4 Nanoparticles Anchored on Nitrogen-Doped Reduced Graphene Oxide as a Multifunctional Catalyst for H_2O_2 Reduction, Oxygen Reduction and Evolution Reaction. *Sci. Rep.* **2017**, *7*, 1−11.
(66) Zhi, J.; Wang, Y.; Deng, S.; Hu, A. Study on the Relation between Pore Size and Supercapacitance in Mesoporous Carbon Electrodes with Silica-Supported Carbon Nanomembranes. *RSC Adv.* **2014**, *4*, 40296−40300.
(67) Zheng, Q.; Zhang, B.; Lin, X.; Shen, X.; Yousefi, N.; Huang, Z. D.; Li, Z.; Kim, J. K. Highly Transparent and Conducting Ultralarge Graphene Oxide/Single-Walled Carbon Nanotube Hybrid Films Produced by Langmuir-Blodgett Assembly. *J. Mater. Chem.* **2012**, *22*, 25072−25082.
(68) Yan, X.; Tian, L.; He, M.; Chen, X. Three-Dimensional Crystalline/Amorphous Co/Co_3O_4 Core/Shell Nanosheets as Efficient Electrocatalysts for the Hydrogen Evolution Reaction. *Nano Lett.* **2015**, *15*, 6015−6021.
(69) Meher, S. K.; Rao, G. R. Ultralayered Co_3O_4 for High-Performance Supercapacitor Applications. *J. Phys. Chem. C* **2011**, *115*, 15646−15654.
(70) Howli, P.; Das, S.; Sarkar, S.; Samanta, M.; Panigrahi, K.; Das, N. S.; Chattopadhyay, K. K. Co_3O_4 Nanowires on Flexible Carbon Fabric as a Binder-Free Electrode for All Solid-State Symmetric Supercapacitor. *ACS Omega* **2017**, *2*, 4216−4226.
(71) Usman, M.; Adnan, M.; Ahsan, M. T.; Javed, S.; Butt, M. S.; Akram, M. A. In Situ Synthesis of a Polyaniline/ Fe-Ni Codoped Co_3O_4 Composite for the Electrode Material of Supercapacitors with Improved Cyclic Stability. *ACS Omega* **2021**, *6*, 1190−1196.
(72) Lin, Z.; Qiao, X. Coral-like Co_3O_4 Decorated n-Doped Carbon Particles as Active Materials for Oxygen Reduction Reaction and Supercapacitor. *Sci. Rep.* **2018**, *8*, 1−10.
(73) Wang, Y.; Lei, Y.; Li, J.; Gu, L.; Yuan, H.; Xiao, D. Synthesis of 3D-Nanonet Hollow Structured Co_3O_4 for High Capacity Supercapacitor. *ACS Appl. Mater. Interfaces* **2014**, *6*, 6739−6747.
(74) Wei, G.; Zhou, Z.; Zhao, X.; Zhang, W.; An, C. Ultrathin Metal-Organic Framework Nanosheet-Derived Ultrathin Co_3O_4 Nanomeshes with Robust Oxygen-Evolving Performance and Asymmetric Supercapacitors. *ACS Appl. Mater. Interfaces* **2018**, *10*, 23721−23730.
(75) Lin, G.; Jiang, Y.; He, C.; Huang, Z.; Zhang, X.; Yang, Y. In Situ Encapsulation of Co_3O_4 Polyhedra in Graphene Sheets for High-Capacitance Supercapacitors. *Dalton Trans.* **2019**, *48*, 5773−5778.
(76) Mukhiya, T.; Ojha, G. P.; Dahal, B.; Kim, T.; Chhetri, K.; Lee, M.; Chae, S. H.; Muthurasu, A.; Tiwari, A. P.; Kim, H. Y. Designed Assembly of Porous Cobalt Oxide/Carbon Nanotentacles on Electrospun Hollow Carbon Nanofibers Network for Supercapacitor. *ACS Appl. Energy Mater.* **2020**, *3*, 3435−3444.
(77) Manohara Babu, I.; William, J. J.; Muralidharan, G. $AgCoO_2$−Co_3O_4/CMC Cloudy Architecture as High Performance Electrodes for Asymmetric Supercapacitors. *ChemElectroChem* **2020**, *7*, 535−545.
(78) Xing, M.; Gao, A.; Liang, Y.; Deng, S.; Shu, D.; Su, S.; Yi, F.; Zhou, X.; Zhu, Z. Defect-Engineered 3D Cross-Network Co_3O_4-XN_xNanostructure for High-Performance Solid-State Asymmetric Supercapacitors. *ACS Appl. Energy Mater.* **2021**, *4*, 888−898.
(79) Jia, W. L.; Li, J.; Lu, Z. J.; Juan, Y. F.; Jiang, Y. Q. Synthesis of Porous Co_3O_4/Reduced Graphene Oxide by a Two-Step Method for Supercapacitors with Excellent Electrochemical Performance. *J. Alloys Compd.* **2020**, *815*, 152373.
(80) Paliwal, M. K.; Meher, S. K. Sedgelike Porous Co_3O_4 Nanoarrays as a Novel Positive Electrode Material for Co_3O_4//Bi_2O_3 Asymmetric Supercapacitors. *ACS Appl. Nano Mater.* **2019**, *2*, 5573−5586.
(81) Liu, B.; Kong, D.; Zhang, J.; Wang, Y.; Chen, T.; Cheng, C.; Yang, H. Y. 3D Hierarchical Co_3O_4@Co_3S_4 Nanoarrays as Cathode Materials for Asymmetric Pseudocapacitors. *J. Mater. Chem. A* **2016**, *4*, 3287−3296.
(82) Kim, S. G.; Jun, J.; Kim, Y. K.; Kim, J.; Lee, J. S.; Jang, J. Facile Synthesis of Co3O4-Incorporated Multichannel Carbon Nanofibers for Electrochemical Applications. *ACS Appl. Mater. Interfaces* **2020**, *12*, 20613−20622.
(83) Liu, X. Y.; Gao, Y. Q.; Yang, G. W. A Flexible, Transparent and Super-Long-Life Supercapacitor Based on Ultrafine Co_3O_4 Nanocrystal Electrodes. *Nanoscale* **2016**, *8*, 4227−4235.
(84) Adhikari, S.; Selvaraj, S.; Ji, S.; Kim, D. Encapsulation of Co_3O_4 Nanocone Arrays via Ultrathin NiO for Superior Performance Asymmetric Supercapacitors. *Small* **2020**, *16*, 2005414.
(85) Zhu, X.; Sun, M.; Zhao, R.; Li, Y.; Zhang, B.; Zhang, Y.; Lang, X.; Zhu, Y.; Jiang, Q. Nanoscale Advances Performance Supercapacitors. *Nanoscale Adv.* **2020**, *2*, 2785−2791.
(86) Shaheen, I.; Ahmad, K. S.; Zequine, C.; Gupta, R. K.; Thomas, A. G.; Malik, M. A. Green Synthesis of ZnO-Co_3O_4 nanocomposite Using Facile Foliar Fuel and Investigation of Its Electrochemical Behaviour for Supercapacitors. *New J. Chem.* **2020**, *44*, 18281−18292.
(87) Haridas, V.; Narayanan, B. N. ScienceDirect One Pot Synthesis of $Co(OH)_2$−Co_3O_4 Mesoporous Nanoarchitecture For Supercapacitor Applications. *Mater. Today: Proc.* **2019**, *9*, 1−6.
(88) Xu, R.; Liu, P.; Ji, G.; Gao, L.; Zhao, J. Versatile Strategy to Design Flexible Planar-Integrated Microsupercapacitors Based on Co_3O_4-Decorated Laser-Induced Graphene. *ACS Appl. Energy Mater.* **2020**, *3*, 10676−10684.
(89) Tao, K.; Yang, Y.; Yang, C.; Ma, Q.; Han, L. Construction of $NiCo_2O_4$ Nanosheet-Decorated Leaf-like Co_3O_4 Nanoarrays from Metal-Organic Framework for High-Performance Hybrid Supercapacitors. *Dalton Trans.* **2019**, *48*, 14156−14163.
(90) Khalaj, M.; Sedghi, A.; Miankushki, H. N.; Golkhatmi, S. Z. Synthesis of Novel Graphene/Co_3O_4/Polypyrrole Ternary Nanocomposites as Electrochemically Enhanced Supercapacitor Electrodes. *Energy* **2019**, *188*, 116088.
(91) Li, Y.; Li, W.; Yang, C.; Tao, K.; Ma, Q.; Han, L. Engineering Coordination Polymer-Derived One-Dimensional Porous S-Doped Co_3O_4 nanorods with Rich Oxygen Vacancies as High-Performance Electrode Materials for Hybrid Supercapacitors. *Dalton Trans.* **2020**, *49*, 10421−10430.
(92) Gao, M.; Wang, W. K.; Rong, Q.; Jiang, J.; Zhang, Y. J.; Yu, H. Q. Porous ZnO-Coated Co_3O_4 Nanorod as a High-Energy-Density Supercapacitor Material. *ACS Appl. Mater. Interfaces* **2018**, *10*, 23163−23173.
(93) Sun, Y. A.; Chen, L. T.; Hsu, S. Y.; Hu, C. C.; Tsai, D. H. Silver Nanoparticles-Decorating Manganese Oxide Hybrid Nanostructures for Supercapacitor Applications. *Langmuir* **2019**, *35*, 14203−14212.
(94) Chen, G. Z. Linear and Non-Linear Pseudocapacitances with or without Diffusion Control. *Prog. Nat. Sci.: Mater. Int.* **2021**, *31*, 792−800.

https://doi.org/10.1021/acsomega.2c06369
ACS Omega 2023, 8, 2183−2196